# 4π Thermography: A projection to Understand Thermal Balance

Jairo Acuña Paz y Miño, Claire Lawrence, Benoit Beckers
Urban Physics Joint Laboratory, Université de Pau et des Pays de l'Adour, E2S UPPA, Anglet, France

## Abstract

The objective of this work is to represent in a compact and synthetic way surface temperatures at different points of interest throughout an urban scene, by building 4π Thermograms.

From a geometrical approach, combining thermography and photographic techniques, a panoramic thermogram is assembled, which enables all directions to be seen from one position. This spherical representation of the data permits to observe the radiative phenomena in a spatialized way allowing its quantification and better understanding. Spatialized distribution of radiation could be expressed as an average temperature weighted by the area of all objects surrounding the measuring point. This emerges as an interesting alternative for measuring the mean radiant temperature in a complex urban scene where multiple heterogeneous surfaces must be considered.

## Introduction

Pedestrian thermal comfort depends on the energy exchanges between him and his environment. Thermal transfer by conduction is, in most of the cases, negligible. The convection exchange – which depends on air temperature, wind speed and relative humidity –, is important. Radiation, however, is of prime importance, especially in the presence of direct solar radiation. But, radiative fluxes are difficult to quantify since each surface acts as an individual source of radiation. This limitation is particularly significant regarding longwave radiation or the "invisible thermometric spectrum", as Herschel (1800) called it. Infrared rays are subject to reflection, transmission and absorption as well as visible light rays. However, a scene observed within the spectral range of 7.5µm to 13µm is not easy to interpret.

To quantify the radiative net exchange, it is necessary to measure and then integrate every surface temperature visible from the measuring point at a particular time. Despite its accuracy, this technique is time consuming and resource expensive (Höppe, 1992). An alternative approach would be to measure the temperature radiation intensity independently of the air velocity by placing radiometers at the measuring point (Richards, 1951; Koch, 1961; Gagge, 1967). These *"active radiometers"* (Berglund, 1977), however, need electrical components to be kept at ambient temperature. Another option is to use a globe thermometer. This device, presented by Vernon in 1930 and considered the first and simplest *"passive radiometer"*, allows to measure globe temperature and calculate the mean radiant temperature ($T_{mrt}$) (Bedford, 1934) by taking into account the air temperature and wind velocity. $T_{mrt}$ is defined as the "uniform surface temperature of an enclosure in which an occupant would exchange the same amount of radiant that as in the actual non-uniform enclosure" (ASHRAE, 2001).

Nevertheless, the scene surrounding the user does not act upon him homogeneously. Some researches include weighting coefficients in order to consider the human shape (Underwood, 1966), but spatialization remains an issue. This aspect, overlooked by the aforementioned methods, may be assessed by means of thermography as shown by Asano (1996) and later improved by Tamura (2001).

Therefore, an interest exists in obtaining spatial information within a scene, either to show the average surface temperature of each element in the scene as the result of a simulation (Nytsch-Geusen, 2017), or to map user's *comfort* with a high level of detail within an occupied space (Teitelbaum, 2017).

Recent technological advances have allowed to manufacture high resolution thermal cameras with additional features at affordable prices, facilitating the entry of this technology into the world of measurement and the built environment. Thermography, often used for building diagnostics, permits other approaches seeking to collect a greater amount of information in a single image, either from aerial or a pedestrian point of view (Beckers, 2019), enabling to calibrate thermal simulations (Aguerre, 2019).

In this paper, a set of individual thermograms are assembled giving way to a 4π thermogram, which provides precise information on the influence of each visible surface of the scene at the measurement point. This explores the advantages of thermography in complex urban scenes.

This method is tested on several locations along a short walk to illustrate the microclimatic diversity from the user's point of view on a compact urban historical district. This work quantifies the longwave radiative component. In order to help designers, urban planners and decision makers get a better grasp of its influence on the scene, results representation has been carefully chosen.


https://doi.org/10.26868/25222708.2019.210969

## Methods

Five 4π thermographs in a compact urban environment illustrate the spatial influence of the scene on the radiative balance at the pedestrian level.

In a time span of 75 minutes and a distance of 240m, the longwave mean radiant flux was measured in 5 different urban configurations. At each of them, relative humidity (HR), air temperature ($T_{air}$) and wind velocity were measured. 4π thermograms and 4π photographs were captured under different weather conditions and at different moments of the day. A single complete measurement session was selected for the results. The globe temperature ($T_g$) was compared with the longwave mean radiant temperature ($T_{LWmrt}$) obtained using the methodology presented in this study.

Longwave radiant temperature was calculated according to Stefan-Boltzmann's law, by integrating the flux density emitted from every direction to the center of a fictive sphere that envelops the point of measurement.

### Longwave measurement set up

A FLIR T460 thermal camera with a spectral sensitivity of 7.5 µm – 13µm and a wide-angle lens (FOV 73° x 90°) was placed at a height of 1.1m above the ground, corresponding to the center of gravity of an average adult (Mayer, 1987). From this position, the thermal scene (4π sr) around this point was captured. The thermal camera was installed on a panoramic mount programmed to place the camera in the 14 positions used to capture the images that were then assembled into a single 4π thermogram (Figure 1). The total capture time is about 150 seconds per location considering that this time is sufficiently short to ignore its effect on the radiant temperature of the scene.

For this study, the emissivity of all objects in the scene was considered as if they were black bodies (ε=1) and the distance from the camera to objects in the scene was considered null. Thus, the automatic correction of the camera for atmospheric transmission was discarded. Under these conditions, temperatures were deduced directly from the radiant flux received by the camera (Kruczek, 2015).

### Calibration and preparation

This section describes the distortions that have been identified in this study and the procedures used to avoid them. The inconsistencies that appear in some images have been explained.

When using a thermal camera as well as a photographic camera, it is necessary to know the characteristics of its optics in order to obtain the right images. In this study the purpose is to assemble several images in a spherical panoramic, therefore, the preparation of the procedure and the camera is imperative to avoid distortion and get an accurate reading of the information of the scene.

### Non-parallax

Parallax is the angular deviation of the apparent position of an object relative to the observation point. In other words, it is the effect of the change of position of the observer on what he observes.

*Figure 1: 4π Thermography device setup: FLIR T460 placed on automatic panoramic-mount.*

To build a 4π thermogram, it is necessary to pivot the camera with each shot in order to capture the whole scene. There is a point on which the camera must rotate to achieve a perfect alignment in each capture. For the sphere, this point is the origin (x=0; y=0; z=0). For the camera, this non-parallax point is the entry pupil.

To locate the non-parallax point, the camera was placed on a panoramic mount fixed on a tripod. The panoramic mount allows the camera to be rotated without having to move the tripod. This allows to adjust the camera position to achieve the desired pivot point. To check the correct alignment of the axes, the camera was placed focusing on a scene where two objects, at different distances from the camera, overlap. From this position and looking through the viewfinder, the camera was rotated in the horizontal plane so that the objects in focus were located at the extremes of the image. When the observed objects remain aligned despite the change in position, the scene is being observed from the non-parallax point. (Littlefield, 2006)

### Lens Distortion

In order to determine the distortion produced by the lens, a sequence of images was captured under sunlight using an alternating pattern of black and white squares, of known dimensions, so that it is visible for the thermal camera. The sequence frames the scene placing the pattern in different regions of the image and with different orientations relative to the camera, since the distortion increases radially from the center of the image.

Using a MATLAB routine (Bouguet, 2015), the coordinates of the vertices of the squares are placed in the image and compared to the estimated position where they should be, if distortion did not affect the image. The algorithm makes it possible to relate 3D world points and their corresponding 2D image points. From this relation, it is possible to determine the rotation and translation of the camera, the extrinsic values and, the focal distance, the input pupil and the skew coefficient, the intrinsic values. This enables to establish the area that is the least affected by radial distortion – barrel distortion – which is used on the further projection.

**Vignetting effect**

An image captured either by a thermal or visible camera usually presents a radial falloff of intensity from the center of the image. This is the *vignetting* effect.

When making thermograms, the vignetting effect affects the image, causing the corners to look warmer than they actually are. This is due to the location of the pixel and a significant temperature difference in the scene, its correction may require sophisticated correction models [Goldman 2010].

Taking into account this information, the capture time and the aperture angle of the lens, it was decided to superimpose each image by about 18% (Figure 3) to decrease the distortion caused by the lens and the vignetting effect, thereby avoiding to correct the images, with the purpose of avoiding any alteration that could tamper the information measured with the camera.

**Partition of the sphere**

To build a $4\pi$ thermogram, it is necessary to use a spherical canvas. The hemisphere partition proposed by Beckers (2014a) was used in this study. It allows the user to select the number of cells while ensuring that each one retains the same solid angle and aspect ratio. This partition provides an easy way of identifying each cell and its position, since its mesh is defined by parallels and meridians. Being an equivalent projection, (or equal-area) facilitates the calculation of view factors.

Mainly used as a celestial vault to calculate daylight availability and shortwave energy budget on an urban scale, in this paper, this partition is duplicated to construct a sphere (Figure 2), which serves to evaluate the entire radiative environment at one point.

The possibility of choosing the number of cells gives the opportunity to try different resolutions. The partition of the sphere into 40000 cells is a good compromise between calculation time and image quality, taking about 1 minute to generate each.

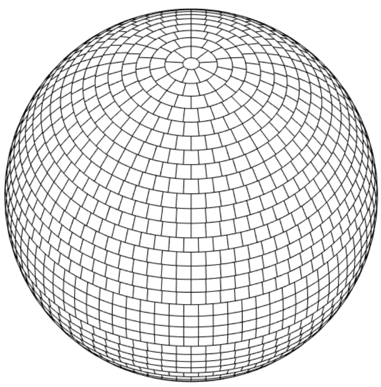

*Figure 2: Partition of a sphere in 2000 equal-area cells.*

**Projection on the sphere**

After calibration and capture of the thermograms, they are assembled into a single thermogram $4\pi$. 7 images build a hemisphere, of which one covers the Zenith (Figure 3), the same process is repeated to complete the sphere.

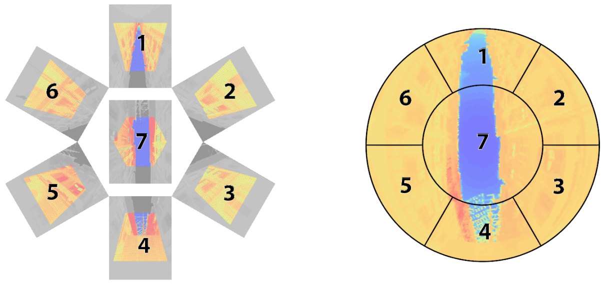


*Figure 3: Construction of the hemisphere using 7 thermograms.*

The position of each thermogram within the sphere was calculated taking into account the field of view (73° x 90°) and the camera positions with an angular resolution of 0.015°. The position of each thermogram is known, so vectors were traced from the origin of the sphere to the center of each thermogram. Thermograms are treated as matrices of values and they are segmented into zones in order to lighten the calculation. Within each zone, the value whose location vector coincides with the center of the corresponding cell was searched and this was projected on the sphere giving as a result a sphere of radiometric values.

**Projection of the sphere**

To be able to observe the radiative scene surrounding a point, it becomes necessary to use a central projection. It can synthesize the scene into a sphere on which the radiative environment is projected. However, the sphere is impossible to unfold. It is therefore necessary to use a cartographic projection to obtain a flat image (Figure 4).

No cartographic projection of the sphere can be both conformal (preserving angles) and equivalent (preserving areas). Moreover, no azimuthal projection can project the entire sphere. Other studies have represented spherical by means of cylindrical projections (Asano, 1996; Tamura, 2001). However, in order to observe spherical thermograms and precisely quantify the impact of each surface of the scene, the Mollweide projection is ideal (Beckers, 2014b).

*Figure 4: Mollweide projection of Cinq Cantons' square spherical photograph.*

The Mollweide projection is a pseudo-cylindrical projection that represents the complete sphere in an ellipse with a ratio of 2:1 between the axes. The meridians are distributed equidistantly, and the latitudes are kept as horizontal lines. Since the Mollweide projection is equivalent, it is possible to directly measure the solid angle of an object from the measurement point (Lapaine, 2011).

**Longwave mean radiant temperature**

In order to quantify the mean radiant temperature, it is necessary to determine the area of each radiative surface around the measurement point. The sky is also one of them. For each surface, it is necessary to determine its emissivity and its reflection coefficient. These depend on the direction.

The mean radiant temperature describes the effect of a complex radiant environment considering diffuse, direct shortwave irradiance ($D_i$ , I) [W m$^{-2}$] and longwave irradiance ($E_i$) [W m$^{-2}$].

The flux received by the pedestrian ($Q_{tr}$) [W m$^{-2}$] is affected by its position and orientation ($F_i$ , $f_p$) with respect to each of the surfaces (i=1, …, n). In addition, it is absorbed in a different manner according to its wavelength ($\alpha_{LW}$, $\alpha_{SW}$) (Höppe, 1992).

$$Q_{tr} = \alpha_{LW} \sum_{i=1}^{n} F_i E_i + \alpha_{SW} \sum_{i=1}^{n} F_i D_i + \alpha_{SW} f_p I \quad (2)$$

In this study, only the longwave component was measured. The longwave radiant mean temperature was calculated by Stefan-Boltzmann's law where σ is the Stefan-Boltzmann's constant ($\sigma = 5.67\text{x}10^{-8}$ [W m$^{-2}$ K$^{-4}$])

$$Q_{tr} = \varepsilon\, \sigma\, T_{LWmrt}^{4} \quad (3)$$

To determine the total flux received at the measuring point, it is necessary to integrate the fluxes emitted by the area of each cell ($\Omega R^2$ [sr m$^2$]) on a sphere of radius R [m$^2$].

$$Q_{tr} = \frac{\sum \varepsilon \sigma\, T^4 \Omega\, R^2}{4\pi R^2} \quad (4)$$

According to $T_{mrt}$'s definition, the radiant energy that affects the pedestrian in a complex environment is equal to that of a black body (ε = 1) isotherm at $T_{mrt}$ [K].

By using an equivalent partition for the sphere, the solid angle of each of its cells is determined by the total number of cells (Npatch).

$$\Omega = \frac{N_{patch}}{4\pi} \quad (5)$$

Therefore, the longwave mean radiant temperature ($T_{LWmrt}$)[°C] is calculated as the mean flux (on the sphere) measured with the thermal camera.

$$T_{LWmrt} = \sqrt[4]{\frac{\sum T^4}{N_{patch}}} - 273.15 \quad (6)$$

Different approaches make it possible to quantify the mean radiant temperature. The use of a globe thermometer is the simplest, however, its spherical shape is a good approximation only for a seated human, its response time is prolonged and considers a single absorption coefficient for the whole spectrum. On the other hand, the integral radiation measurement (Lindberg 2008) uses 3 net radiometers to measure hemispheric fluxes in 6 orientations (the 4 cardinal points, the upper and lower hemisphere) rotating 90° in each case and with a resolution of 3 minutes. This method allows to consider different absorption coefficients for long-waves and for short-waves. In addition, it allows to multiply the fluxes by weighting values to approximate a standing person.

The $4\pi$ thermography makes it possible to identify and quantify the radiation sources in each scene. Starting from a geometric approach, the weighting of each cell on the sphere by different angular factors is presented as a simple solution to approximate the orientation and position of the pedestrian.

**Study case**

The study was carried at the historical district of Bayonne, at the south of France, during winter.

**Selection of points of interest**

This study concerns the pedestrian, therefore the points of interest have been selected to observe how the urban configuration and design affects the thermal environment of the user (Figure 5). The 5 configurations meet the following conditions:

1. Interior - solid - "opaque"
2. Semiexterior – with different materials
3. Exterior - intersection of several streets
4. Exterior - narrow street
5. Exterior - open air

The measurements were made on December 29th, 2018, taking into account the weather conditions. The hour of the mesurement between 14:00 and 15:15, was chosen taking into account that this is the period of the day where the presence of the pedestrian in the street is most significant. Therefore, it is also the period where the study of the influence of the radiative environment on the pedestrian is of greatest interest.

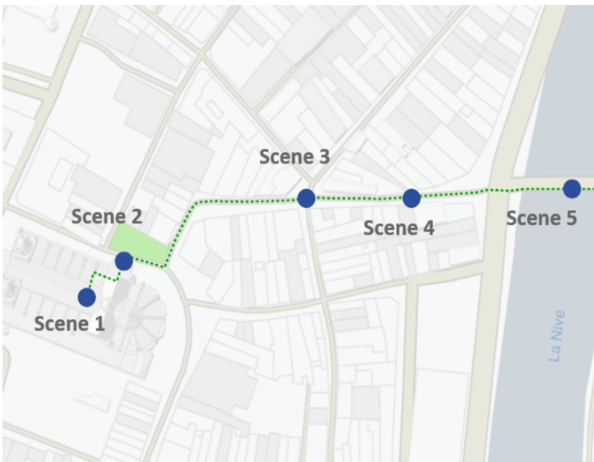


*Figure 5: Chosen points of interest in the center of Bayonne.*

## Results and observations

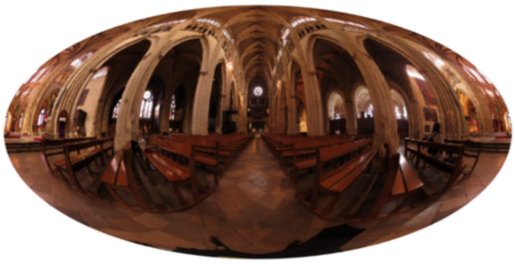

*Figure 6: Mollweide projection of 4π photograph inside the Cathedral of Bayonne.*

The first measurement is inside the Cathedral of St. Mary of Bayonne, (Figure 6) a 13th century Gothic cathedral. The image was taken at 14h00 (Figure 7), at this moment, lighting conditions inside the Cathedral are unfavorable for the photograph, but this has no impact on the thermogram. The spatialization of thermal information allows distinguishing the contributions coming from people who occupied the scene during the measurement, from those coming from the built environment. This scene presents homogeneous apparent temperatures, where the difference is less than 5° C. This thermal behavior is due to the low short-wave radiation and significant thermal inertia of the massive stone walls and structure of the building. The air temperature associated with a weak convection coefficient, caused by its low velocity, slowly heats the surfaces. As a result, the globe temperature approaches the air temperature followed by the longwave mean radiant temperature.

Despite being a homogeneous scene, it is possible to distinguish the slight temperature difference between the left and right side of the image. The left side shows a somewhat higher temperature, because it corresponds to the southern facade of the cathedral which has been exposed to the sun throughout the day.

The second scene is under the Cathedral entrance, at Pasteur Square (Figure 8). The sky was cloudy, and the wind speed was low at the instant of measurement. Due to the presence of solar radiation (diffuse), the globe temperature rises above the air temperature leaving the longwave mean radiant temperature at the bottom. It is possible to observe, in the center of the image, the stone structure at a uniform temperature. This contrasts with the heterogeneous temperatures of the neighboring buildings. This includes walls of different thicknesses and glazed surfaces. The thickness and density of the material affect the thermal mass of the objects in the scene, whereas its surface characteristics, color and roughness affect the proportion of the transmitted, reflected and absorbed radiant flux with respect to the incident one (Figures 7 - 11). This can be observed by means of thermography.

For shortwave radiation, the color of the surface has a direct relation with its reflection coefficient. The impact of reflection on sun gains in a compact urban district has shown that rehabilitation at an urban scale is possible through architectural decisions (Beckers, 2018).

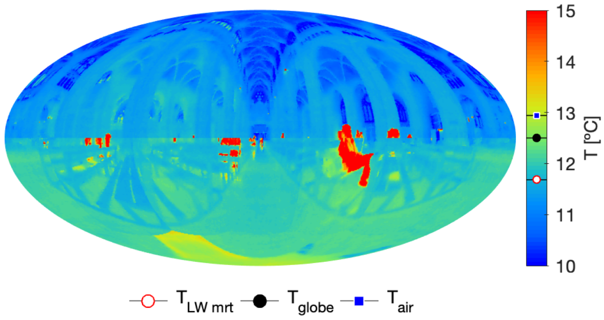


*Figure 7: Scene 1 - Inside the Cathedral of Bayonne.*

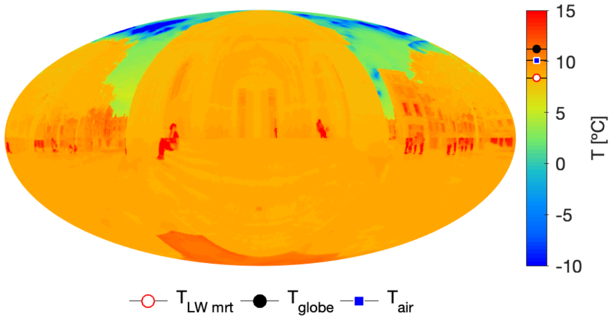


*Figure 8: Scene 2 - Pasteur Square.*

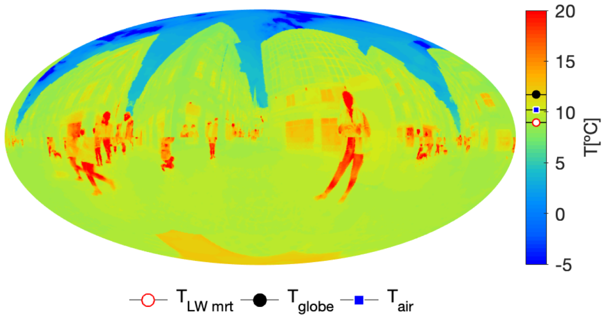


*Figure 9: Scene 3 - Cinq Cantons' Square.*

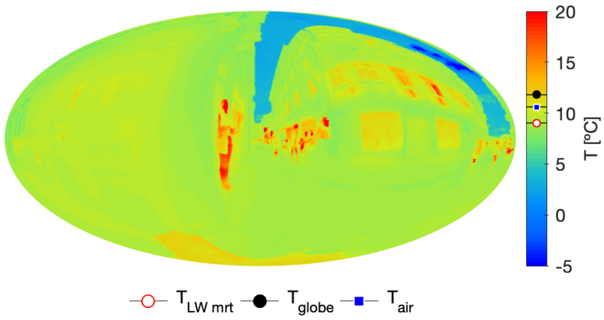


*Figure 10: Scene 4 - Port de Castets' Street.*

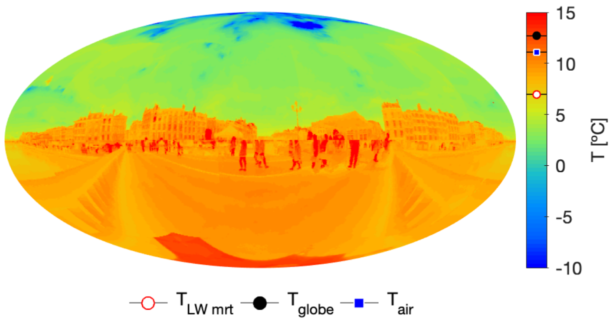


*Figure 11: Scene 5 - Marengo Bridge.*

The colors and composition of the façade is of great importance, especially in the base of narrow urban canyons due to restricted access to natural lighting and solar inputs.

For longwave, reflection its related to surface roughness. A polished metal surface produces specular reflection within both the visible and infrared spectrum. However, a rough surface can produce a diffuse reflection for the visible part of the spectrum and a specular reflection for the infrared spectrum (Figure 4, Figure 9) (Vollmer, 2010). This behavior is due to the relationship between surface roughness and the wavelength of the incident radiation.

The third scene shows the intersection of 5 streets in Cinq Cantons Square (Figure 9), where each street has a different orientation. In this image it is possible to observe that facades exposed to direct solar radiation have higher temperatures. The same surfaces show a decrease in temperature relative to the height of the façade. This is explained by the increase in the sky view factor. As the façade rises, the sky cools it.

The fourth scene depicts a narrow street, where the sky view factor clearly affects the temperature of the facades (Figure 10). Air temperature and globe temperature in this scene have a difference of 1.20°C. In this image, it can be seen that apartments with a deficient insulation could act as thermal inputs towards the outdoor. In this case, the hot spots below the windows of the first floor of the building of the North façade (on the right side) can be observed. These correspond to the radiators mounted on the inside of the façade.

The fifth scene was captured over the Marengo Bridge under a fairly clear sky (Figure 11). Through spatialization of the thermal information, it can be observed why the globe temperature overestimates the values at the poles since it can be seen that for a sphere, the ground has great importance since it represents almost 90% of the lower hemisphere. Likewise, in the open air, the sky occupies almost the entire higher hemisphere. In this image, the presence of the sky has great importance. On the one side, it is the source of heat due to solar radiation in short waves. On the other side, it is a great source of losses by the terrestrial radiation in long waves (towards the sky). The spectral sensitivity (7.5-13 µm) of the camera causes the measured radiant temperature of the sky to be lower than the real temperature of the sky (Takagi, 1967).

*Table 1: Summary of measured data at each scene.*

| Location | $T_{air}$ [°C] | $T_{globe}$ [°C] | $T_{LW\ mrt}$ [°C] | HR [%] | Wind speed [m s$^{-1}$] |
|---|---|---|---|---|---|
| Cathedral of Bayonne | 12,94 | 12,50 | 11,68 | 69,90 | 0,08 |
| Pasteur Square | 10,10 | 11,20 | 8,36 | 69,61 | 0,69 |
| Cinq Cantons' Square | 10,20 | 11,70 | 8,96 | 67,01 | 0,92 |
| Port de Castets' Street | 10,60 | 11,80 | 9,03 | 70,57 | 0,15 |
| Marengo Bridge | 11,10 | 12,70 | 6,97 | 74,26 | 0,14 |

## Discussion and perspectives

As discussed in this study, the radiative environment is of great importance to the pedestrian and the behavior of its infrared component is not intuitive.

In the urban scene, the measurement of radiative flux is an enormous challenge due to the complex morphology of the environment. Here, all surfaces act as radiators bringing to the scene different amounts of radiant energy depending on their temperature, emissivity and position regarding the pedestrian. For this reason, $T_{mrt}$ is one of the most important factors for thermal comfort in urban environments and yet one of the most problematic (Kantor, 2011). The radiative environment has great influence on microclimates. These can vary considerably within the same weather conditions and in certain cases can explain the perception by the pedestrian.

Figure 12 shows the 3 temperature measurements performed in each of the 5 configurations presented in this study. In the first one, indoor, the temperature of globe is below the temperature of the air and above the longwave mean radiant temperature. This is explained by the low radiation in short waves. At this scene, the longwave radiant temperature controls the environment. The inertia of the materials in the scene causes a delay regarding air temperature. The next three measurements were taken outdoor where the portion of visible sky results in a short-wave contribution, even with overcast skies. This brings the globe temperature above the air temperature while the radiant temperature remains below. In the last one, in the open air and over the Nive river, the radiant temperature is the lowest and the gap between it and the globe temperature is the largest. This is mainly explained by the important presence of the sky.

When comparing air, globe and longwave mean radiant temperature, it is possible to observe patterns that relate to these different radiative environments. However, the globe temperature of the scene over the bridge and the first scene -an interior- are very similar, which hinders result interpretation and limits any subsequent evaluation if no spatial information is provided.

The visualization of these radiative microclimates offers the possibility to understand them and their influence on the pedestrian's perception over the thermal scene.

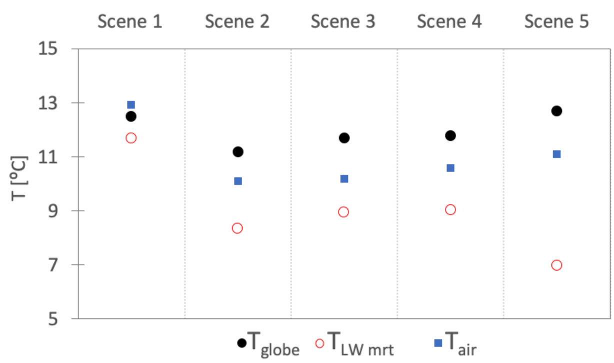


*Figure 12: Air, globe and longwave mean radiant temperatures.*

## Conclusion

Despite the differences in wavelength, thermal and visible radiation are driven by the same physical laws. However, the behavior of the objects seen on the infrared waveband is less intuitive. Therefore, it appears as a new world for the observer, who needs appropriate methods to understand the phenomena.

The human being perceives infrared radiation as heat coming from each surface on the scene. To describe this *radiative environment* as a whole, a strategy to study the scene around one point by 4π thermography has been developed. This approach allows to visualize the radiative phenomena while preserving the details of the scene. Other methods used to study the surroundings of a chosen point may fail to provide precise spatial information, 4π thermograms are then an efficient alternative in these cases since accurate information is obtained by passive data recollection.

The Mollweide projection has proved to be an effective way to represent the whole environment, accordingly to the geometric laws governing thermal exchanges.

Results show that environments where the air, globe and longwave mean radiant temperatures are almost equivalent, are be most probably found indoor.

If shortwave radiation is significant, it becomes the driving factor on the balance - such as in exteriors, under sunny conditions-. In this case, globe and longwave mean radiant temperature show major differences, being globe temperature the highest one.

In turn, when longwave radiation governs the scene, the presence of shortwave radiation is null and low wind speeds are registered. In this case, longwave mean radiant temperature depends mainly on two factors: The temperature difference between the interior and the exterior, and the thermal inertia of the bounding material.

Using a spatialized distribution of radiation has revealed to be an interesting alternative to understand the radiative phenomena's influence on the urban thermal balance.

It has been shown that some scenes with differentiated environments may exhibit nearly the same globe temperature, which hinders results interpretation impeding any subsequent assessment. Through the method here proposed it is possible to recognize each source of radiation in the scene and its influence over the point of measure, permitting to go beyond bare quantification. This method may be therefore a useful tool for decision makers and urban planners.

## References

Aguerre, J., Nahon, R., Garcia-Nevado, E., La Borderie, C., Fernández, E., Beckers B. (2019). A street in perspective: Thermography simulated by the finite element method. *Building and Environment 148* (15), 225-239.

Asano, K., Hoyano, A. & Matsunaga T. (1996). Development of an urban thermal environment measurement system using a new spherical thermography technique. *Proceedings from SPIE 2744, Infrared Technology and Applications XXII*. Orlando (USA), 27 June 1996.

ASHRAE, (2001). *Fundamentals Handbook (SI Edition) Chapter 8: Thermal Confort.*

Beckers, B. & Beckers, P. (2014a). Sky vault partition for computing daylight availability and shortwave energy budget on an urban scale. *Lighting Research and Technology 46* (6), 716-728.

Beckers, B. & Beckers, P. (2014b). *Reconciliation of Geometry and Perception in Radiation Physics.* John Wiley and Sons, Inc.

Beckers, B., Acuña Paz y Miño, J. & Lawrence, C. (2018). How can reflected light modify solar gains in a compact urban district?. *Proceedings from WREN-WREC: World Renewable Energy Congress.* London, (UK), 30 July - 3 August 2018.

Beckers, B., Aguerre, J., Besuievsky, G., Fernández, E., Garcia-Nevado, E. & La Borderie, C. & Nahon. R. (2019). Visualizing the Infrared Response of an Urban Canyon Throughout a Sunny Day. In Sayigh A. (eds) *Sustainable Building for a Cleaner Environment. Innovative Renewable Energy*. Springer, Cham, 276-284.

Bedford, T. & Warner. C. G. (1934). The Globe Thermometer in Studies of Heating and Ventilation. *Journal of hygiene 34*(4), 458-73.

Berglund, L. G. (1977). Radiation Measurement for Thermal Comfort Assessment. *SP491 Built Environment. Symposium at the National Bureau of Standards*, 117-134. September 1977.

Bouguet, J. Y. (2015). "Camera Calibration Toolbox for Matlab." Computational Vision at the California Institute of Technology.

Gagge, A. P., Stolwick, J. & Hardy, J. D. (1967). Comfort and Thermal Sensations and Associated Physiological Responses at Various Ambient Temperatures. *Environmental Research 1*(1), 1-20.

Goldman, D. B. (2010). Vignette and Exposure Calibration and Compensation. *IEEE Transactions on Pattern Analysis and Machine Intelligence 32*(12), 2276-2288.

Herschel, W. (1800). Experiments on the Refrangibility of the Invisible Rays of the Sun. *Philosophical Transactions of the Royal Society of London 90*, 284-292.

Höppe P.(1992). Ein neues Verfahren zur Bestimmung der mittleren Strahlungstemperatur in Freien. (A new measurement procedure to obtain the mean radiant temperature outdoors). *Wetter und Leben 44*, 147-151.

Kántor, N. & Unger, J. (2011). The most problematic variable in the course of human-biometeorological comfort assessment – the mean radiant temperature. *Central European Journal of Geosciences 3*(1), 90-100.

Koch, W. (1961). A Method of Calibrating Two-Sphere Non-directional Radiometers. *Nature 192* (4806), 960-960.

Kruczek, T. ( 2015). The effective sky temperature: An enigmatic concept. *Heat and Mass Transfer 47*(9), 1171-1180.

Lapaine, M. (2011). Mollweide Map Projection, KoG-15, 7-16.

Lindberg F., Holmer B. & Thorsson S. (2008). SOLWEIG 1.0 – Modelling spatial variations of 3D radiant fluxes and mean radiant temperature in complex urban settings. *International Journal of Biometeorology 52*(7), 697-713.

Littlefield, R. (2006). Theory of the “No-Parallax” Point in Panorama Photography.

Mayer, H. & Hoppe, P. (1987). Thermal comfort of man in different urban environments. *Theoretical and Applied Climatology 38*(1), 43-49.

Nytsch-Geusen, C., Ayubi, T., Möckel, J., Rädler, J. & Thorade, M. (2017). BuildingSystems_VR – A new approach for immersive and interactive building energy simulation. *Proceedings from the 15th IBPSA: Conference of International Building Performance Simulation Association*. San Francisco (USA), 7-9 August 2017.

Richards, C. H., Stoll, A. M., & Hardy, J. D. (1951). The pan-radiometer: An absolute measuring instrument for environmental radiation. *Review of Scientific Instruments 22*, 925-934.

Takagi, T. & Matsui, M. (1967). Spectral Radiance of Sky and Terrain in the Middle Infrared Region. *Journal of the Spectroscopical Society of Japan 3* (16), 112-118.

Tamura, T., Hoyano, A., Aoki, H. & Asano, K. (2001). Developing the Capturing System of Spherical Termograph and Applications to Built Environment. *Proceedings from SPIE 4360, Thermosense XXIII,* Orlando (USA), 23 March 2001.

Teitelbaum, E., Guo, H., Read, J. & Meggers, F. (2017). Mapping Comfort with the SMART ( Spherical Motion Average Radiant Temperature ) Sensor. *Proceedings from the 15th IBPSA: Conference of International Building Performance Simulation Association*. San Francisco (USA), 7-9 August 2017.

Underwood C. R. & Ward E. J. (1966). The solar radiation area of man. *Ergonomics 9*, 155-168.

Vollmer, M. & Mollmann, K.P. (2010). *Infrared Thermal Imaging Fundamentals, Research and Applications.* Wiley-VCH Verlag GmbH & Co. KGaA. Weinheim (Germany).